Dynamic mode decomposition-based reconstructions for fluid-structure interactions: An application to membrane wings

Eduardo Rodríguez-López[1], Douglas W. Carter[1], & Bharathram Ganapathisubramani[1]†

†: Corresponding author: g.bharath@soton.ac.uk
[1]: Department of Aeronautical & Astronautical Engineering, University of Southampton, Southampton SO17 1BJ, UK

Keywords

Low-order modelling. Flow-structure interaction. Membrane wings. Linear models.

Abstract

Four data-driven low-order modelling approaches, Dynamic mode decomposition (DMD) and three other variations (optimal mode decomposition, total-least-squares DMD and high-order DMD), are used to capture the spatio-temporal evolution of fluid-structure interactions. These methods are applied to experimental data obtained in a flow over a flexible membrane wing and its elastic deformation. Spectral coherence indicates there exists an interaction between the flow and structural deformation at a single frequency for this problem (depending on the angle of attack and/or the presence of a ground). It is therefore an ideal data set to assess the performance of the four different methods in terms of the relevant modes/frequencies and reconstruction of flow and structural deformation. We show that the four methods detect the same dominant frequency (within Fourier resolution) and qualitatively the same associated mode. However, the modes appear to be heavily damped or amplified preventing a successful flow and structure reconstruction (except when using high-order DMD). This problem persists even if the damping coefficients are set to 0 due to imprecision in the estimation of the dominant frequency. The reconstruction is assessed by means of the average correlation between the real and reconstructed fields corresponding to 0.42 and 0.85 for the fluid and membrane deformation respectively when using high-order DMD (and virtually 0 for the other three methods). Based on the analysis, we conclude that high-order DMD, particularly for when fluid and structural data are modeled simultaneously, is the most suitable method to generate linear low-order models for fluid-structure interaction problems. Further, we show that this modeling is not dependent on the relative energies of fluid and membrane deformation.

1 Introduction

Low-order modelling in fluid dynamics has undergone a shift through the introduction of Dynamic Mode Decomposition (DMD) by Schmid (2010). In contrast to previous methods based on proper orthogonal decomposition (POD; Berkooz et al., 1993), which only provide spatial information of the dominant modes of the flow, DMD associates these spatial modes with a single temporal frequency and decay/growth rate. Consequently, modes are orthogonal in time. Additionally, the method only requires information of time-resolved snapshots and no information is required about the underlying equations describing the physical phenomena. These two facts have captured the attention of the fluid-dynamics community and its application to flow problems has become widespread since its introduction.

In general, any DMD-based methodology seeks two elements: a suitable linear subspace onto which to project the flow snapshots and the linear description of the dynamics in that subspace. The DMD method by Schmid (2010) takes that subspace to be the POD modes and the dynamics are approximated by the evolution from the snapshot at time t to the next snapshot at time $t + \Delta t$. A number of modifications of this basic methodology have been proposed over the last few years. Wynn et al. (2013) proposed to perform a numerical optimization to find an optimal projection space instead of the POD modes. Whilst keeping the POD modes as projection subspace, Dawson et al. (2016) suggested to modify the way in which the dynamics are estimated to account for measurement noise. More recently, Le Clainche and Vega (2017) have generalized the DMD algorithm to include a larger number of snapshots from previous time steps.

DMD and related methods are often used to identify the dynamics of the flow. That is, they aim to obtain the spatial structure of the dominant flow modes and their corresponding frequency and damping/growth rate. This analysis provides an excellent means to describe or understand a large number of the flow problems (c.f. Rowley and Dawson 2017 and references therein). However, not so much attention has been paid to flow reconstruction. In this context, we refer to flow reconstruction as the ability of the method to reconstruct snapshots based on a linear combination of the modes and their frequencies. A successful reconstruction is more demanding than a qualitative description of the flow phenomena hence it requires better accuracy in the estimation of modes' shapes and frequencies. In fact, Dawson et al. (2016) showed that the damping coefficient and frequencies in these methodologies are often not correctly estimated due to noise in the measurements. These inaccuracies may not be a problem to describe the flow but they definitely hinder flow reconstruction.

Considering now the type of problems that can be solved by these methodologies; most of the applications are focused on the description of fluid flows, probably due to the inherent difficulty in understanding them. Nevertheless, note that these methods do not require any knowledge of the physics involved. They could therefore be easily applied to other problems such as fluid-structure interactions (FSI). However, in the context of FSI, these methodologies have only been applied to either the flow (see table 3 of Rowley and Dawson, 2017) or the structural vibrations (Bozkurttas et al., 2009; Kim et al., 2013) separately, but not to both of them simultaneously. Recently, Goza and Colonius (2017) proposed a combined methodology to study FSI problems by means of POD and DMD. However, their study was only focused on identifying the flow dynamics but none of the reconstruction results were presented.

In summary, DMD and other variants have been primarily concentrated in the description of flow problems but not in flow reconstruction. Recently, some DMD-based reconstructions were reported by Menon and Mittal (2020) for simulations of a pitching aerofoil. However, to our knowledge DMD reconstructions and variants thereof have not been thoroughly investigated to model FSI. Consequently, in the present study, the aim is to discuss the suitability of these methodologies to reconstruct FSI problems. In particular a set of low-order models of the flow and the elastic deformation of a membrane wing are presented.

Flexible membrane wings present a novel solution for improving the performance of small/micro air vehicles. The flow around these wings is modified due to the coupling with the elastic membrane which entails improved flight performance at relatively low and transitional Reynolds numbers (1000 to 100,000). In particular, they are shown to delay stall at large angles of attack due to the formation of a leading-edge vortex which is shed and convected downstream (Rojratsirikul et al., 2011). They can be used for flow control, for instance, active camber adjustment (Curet et al., 2014; Buoso and Palacios, 2016; Barbu et al., 2017). In this context, the role of the leading edge vortices is especially significant due to its relationship with the aerodynamic performance. Additionally, control algorithms may benefit from a low-order model of the flow which enables the problem to be reduced to a few degrees of freedom.

The structure of the paper is as follows: Section 2 describes the experimental setup and analyzes the coupling between the flow and the membrane deformation to assess the suitability of this problem to be described by a low-order model as proposed. Section 3 describes briefly the various DMD-like algorithms that will be considered. Section 4 shows the results of the study: the low-order models are applied separately to the fluid and structure and their results discussed in terms of description of the flow and structural deformation (section 4.1) and, more importantly, their reconstruction (section 4.2). These results will be then compared with the combined approach in which we consider flow and membrane deformation simultaneously (section 4.3). Finally, the conclusions of the study are drawn in section 5.

2 Experimental set-up and data reduction

2.1 Experimental set-up

A link to the experimental dataset of the flow-structure dynamical coupling between the membrane-wing deformation and the flow field can be found in Bleischwitz et al. (2017). Although the complete details can be found in Bleischwitz et al. (2015, 2016, 2017), a brief summary of the most important parameters is compiled below.

The membrane wing was designed with a chord $c = 100\,\mathrm{mm}$ and a wingspan of 200 mm resulting in an aspect ratio of 2. The flexible wings were constructed using a latex membrane attached to a steel frame. The latex sheet had a thickness of $t_m = 0.2\,\mathrm{mm}$ density of $\rho_m = 1\,\mathrm{g/cm^3}$ and Young's Modulus of $E_m = 1.5\,\mathrm{MPa}$. The membrane was wrapped around the perimeter steel frame and attached to itself with a 5 mm wide double side tape. The wind-tunnel speed was set to $U_\infty = 8.4\,\mathrm{m/s}$ reaching a Reynolds number based on the wing chord of $Re = 56000$. At this speed, the freestream turbulence of the wind tunnel was less than 0.1%.

The dataset consists in simultaneous measurement of the flow around a membrane by means of particle image velocimetry (PIV) and measurements of the membrane deformation by means of stereoscopic digital image correlation (DIC). Both techniques were synchronized at a frequency of 800 Hz and a total of 5000 images were acquired over a period of 6.25 s. The spatial resolution of the DIC technique is $0.03c$ and its accuracy is

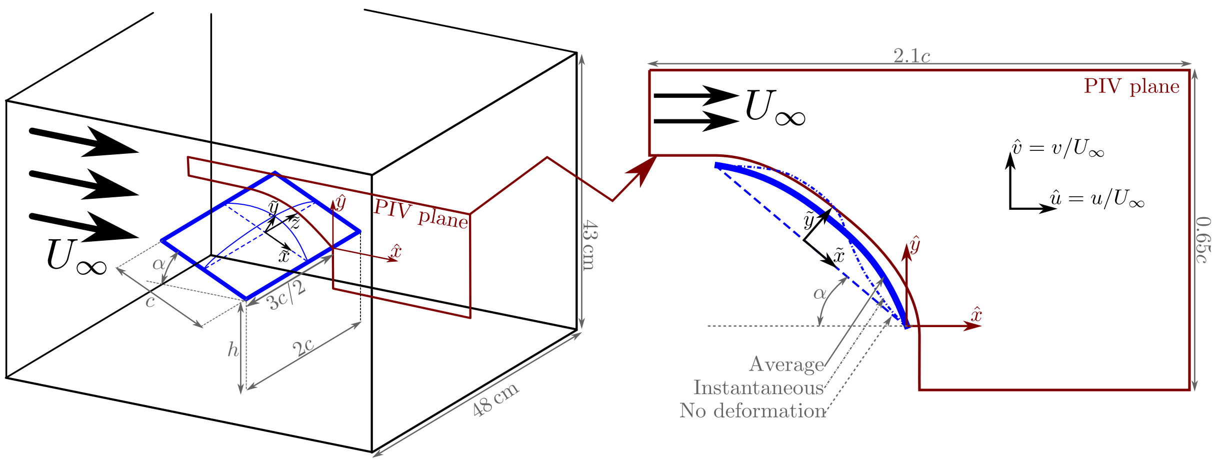

Figure 1: Sketch (not to scale) of the experimental set-up and the coordinate systems. The amplitude of the instantaneous membrane deformation is exaggerated for illustration.

estimated to be better than $0.001c$. PIV is conducted at quarter-span in a streamwise/wing-normal plane. Two cameras are employed in a side-by-side arrangement. After image stitching and multipass post-processing the final resolution is 1.47 mm with a vector spacing of $0.016c$ due to the overlap between the PIV interrogation windows.

The original study focused on three angles of attack ($\alpha = 10°$, $15°$ and $25°$) and three heights over the ground ($h/c = 0.1$, 0.25 and 2) in order to test the membrane wings with and without ground effect. It was found that the strongest fluid-structure coupling was achieved with ground effect ($h/c = 0.1$) at moderate angle of attack ($\alpha = 15°$). A similar coupling was found for a larger angle of attack ($\alpha = 25°$) in free-flight conditions ($h/c = 2$). Consequently, these two cases will be presented below. Throughout this article these two cases will only be referred to by using the angle of attack α, however it should be noted that in the largest $\alpha = 25°$ the wing is in free-flight conditions whilst for $\alpha = 15°$ there is a considerable ground effect ($h/c = 0.1$).

The flow coordinate system x and y is defined as the streamwise and vertical coordinates with origin in the trailing edge ($x_{te} = y_{te} = 0$). Analogously $u = U + u'$ and $v = V + v'$ are the instantaneous velocities in the x and y directions decomposed in their mean (U, V) and fluctuations (u', v'). Magnitudes expressed with a caret are normalized using the chord length and/or the freestream velocity, e.g. $\hat{x} = x/c$, $\hat{y} = y/c$ for coordinates or $\hat{U} = U/U_\infty$, $\hat{V} = V/U_\infty$ for velocities. The sub-index rms will be used to indicate the root-mean-square level.

Note that the previous coordinate system is oriented with $\hat{x}$ parallel to the freestream and $\hat{y}$ normal to it. In order to study the membrane deformation it is more natural to consider the coordinate system in the membrane plane. Coordinates in the membrane plane normalized with the membrane chord will be designated with a tilde: $\tilde{x} = x_{mem}/c$, $\tilde{y} = y_{mem}/c$ and $\tilde{z} = z_{mem}/c$ represent the membrane-parallel, membrane-normal and spanwise directions respectively. Note that the plane $\tilde{x} - \tilde{z}$ is defined without considering mean membrane deformation. A sketch of the coordinate system and other experimental parameters can be found in figure 1.

The original flow field extended until $1.2c$ downstream of the trailing edge and $0.8c$ in the vertical direction. However, as the present study is mainly focused on the fluid-structure interaction, only a subset of this field of view will be considered such that $-1 \leq \hat{x} \leq 1.1$ and $-0.1 \leq \hat{y} \leq 0.55$. Furthermore, the flow in the pressure side of the membrane will be discarded, as within this region the PIV correlation values were significantly smaller and hence the uncertainty in the measurements considerably larger. For the membrane deformation, the 5 mm next to the steel frame were discarded to eliminate the deformations influenced by the tape that held the membrane.

2.2 Preliminary data analysis

Figure 2 shows the mean and root-mean-square velocities for both angles of attack. The mean deformation of the membrane is also shown. A direct comparison between the degree of camber of the membrane is difficult due to the change in both angle of attack and ground effect. In any case, it is clear that the membrane mean curvature adapts to the flow which, in turn, delays the onset of stall (Bleischwitz et al., 2017). In fact, only a small region of the flow seems to be detached in the larger α case.

The largest magnitudes of the vertical velocity fluctuation ($\hat{v}'_{rms}$) are concentrated in the wings' wake likely due to the leading edge vortices being convected downstream. The largest magnitude of the horizontal velocity fluctuation ($\hat{u}'_{rms}$) is located close to the leading edge in the shear layer forming between the wing's wake and the freestream.

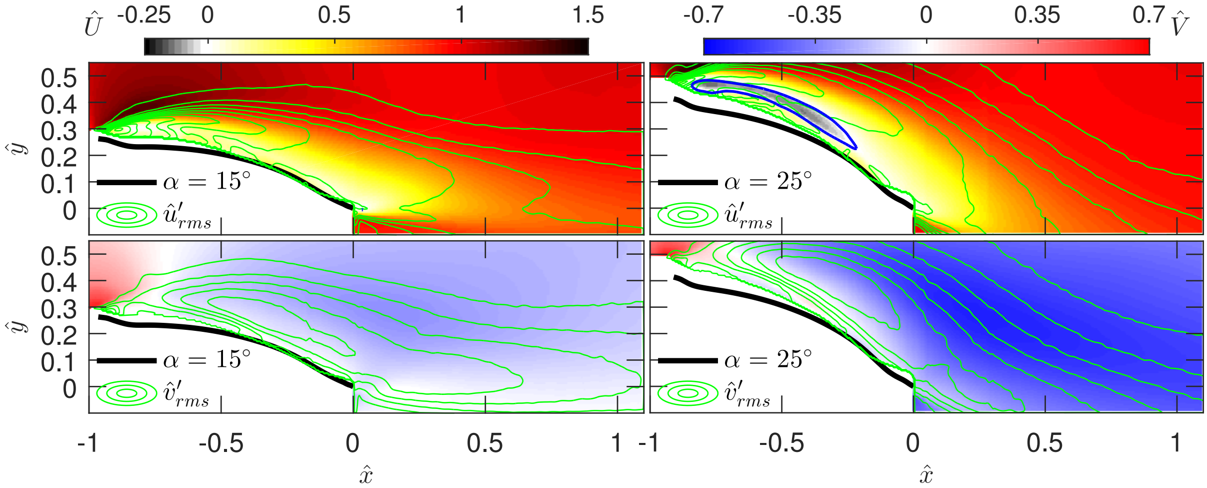

Figure 2: Colormaps of normalized mean streamwise (top row) and vertical (bottom row) velocities for two angles of attack. The superimposed contour lines correspond to the normalized root-mean-square velocity from 0.05 in steps of 0.05. The closed blue contour represents the region of recirculating ($\hat{U} < 0$) flow. Note that contours that intercept the membrane position do not correspond to PIV points, and are the result of forcing specific contour levels that wrap around the PIV domain.

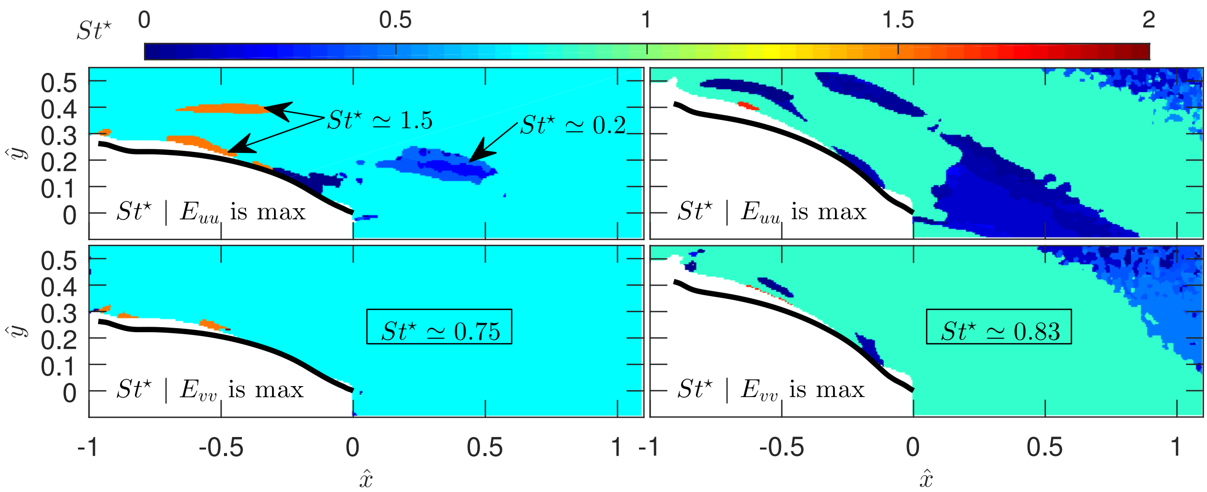

Figure 3: Strouhal number corresponding to the peak of the power spectral density for the two angles of attack.

By analysing the vertical velocity fluctuation at a series of point in the wings' wakes, Bleischwitz et al. (2017) showed that, downstream of membrane wings, there is a distinct peak in the spectral content of $\hat{v}'$. This peak was associated with the periodic shedding of the leading edge vortices. Whereas the intensity of the peak was shown to decrease with streamwise distance its frequency f seemed to be at a constant $St = fc/U_\infty \approx 0.75$ for the $\alpha = 15°$ case.

Given that there exists a clear spectral peak at a certain Strouhal number; rather than showing spectral content at a few discrete points, the Strouhal number $St^\star$ at which the power spectral density is maximum is presented. This is done for the streamwise E_{uu} or vertical E_{vv} velocity fluctuations. The power spectral density is calculated taking the average of 5 windows multiplied by a Hann window to avoid spectral leakage. This provides a frequency resolution of 0.8 Hz.

Figure 3 shows the peak Strouhal $St^\star$ at both angles of attack. The differences between the streamwise and vertical spectra are clearly observed here. E_{vv} exhibits a clear peak which is at a constant Strouhal (within frequency resolution) throughout the flow field. Although there are few spots closer to the wing in which this is not the case, this can be attributed to either noise in the PIV measurements close to the wing, or the influence of the wing's boundary layer and leading-edge formation region. Following Bleischwitz et al. (2017), it is reasonable to assume that this frequency is generated by periodic formation and shedding of vortices from the leading edge. Whilst the $\alpha = 15°$ presents $St^\star = 0.75$; the $\alpha = 25°$ case indicates a higher peak of $St^\star = 0.83$.

In contrast, the streamwise spectra E_{uu} presents distinct dominant frequencies in other regions. As was reported above, the larger fluctuations originated in the shear layer between the wing's wake and the freestream. This shear layers appears to have a higher frequency peak than that corresponding to the leading edge vortex. This is consistent with an incipient shear layer in which the typical eddies are smaller hence their frequencies are higher. It is interesting to note that, particularly for the $\alpha = 15°$ case, in this region the peak frequency for E_{uu} is twice that of E_{vv}. This is consistent with what is observed in the wake of a cylinder (e.g. Zheng and Zhang, 2008) where the coefficient of drag oscillates at twice the frequency as the lift coefficient. In the trailing region, a less evident second shear layers appears between the wings' wake and the laminar flow under the wing. These two shear layers seem to merge at approximately $\hat{x} \approx 0.3$ $\hat{y} \approx 0.2$ in the $\alpha = 15°$ case and $\hat{y} \approx 0.1$ for the $\alpha = 25°$ case. The spectra in this region peaks at a lower frequency, perhaps due to the flapping of both shear layers close to their merging point. As evidenced by the streamwise spectral content, two regions of the flow can be distinguished: the core of the wake sharing the same peak frequency as the vertical fluctuations and another region in which the unsteady shear produces differing dominant frequencies.

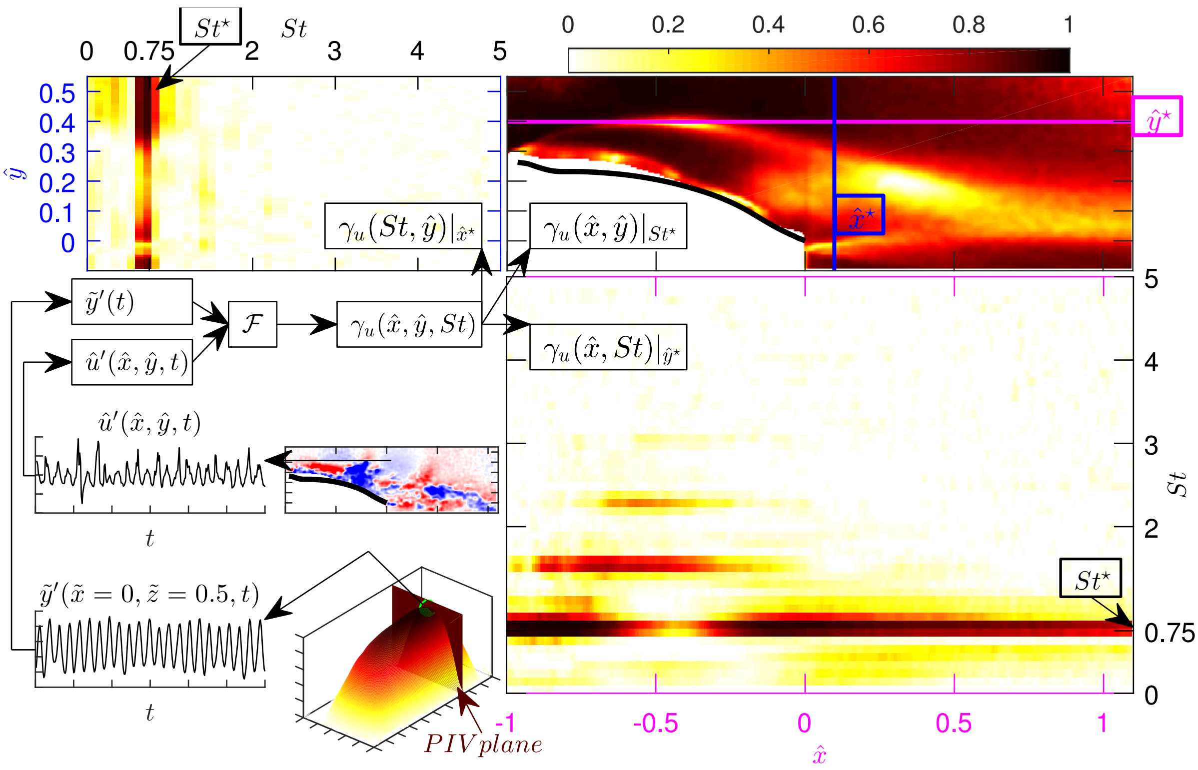

Figure 4: Bottom left corner: sketch of the methodology to obtain the coherence $\gamma(\hat{x}, \hat{y}, St)$. The other three plots are two-dimensional cuts of $\gamma(\hat{x}, \hat{y}, St)$ at $\hat{x} = \hat{x}^\star$, $St = St^\star$ and $\hat{y} = \hat{y}^\star$ (respectively in clockwise direction) for $\alpha = 15°$.

Spectral results suggest that a large part of the flow field is strongly influenced by the leading edge vortices. Further, Bleischwitz et al. (2017) showed a correlation between the flow field and the membrane deformation. However, only results of the mean correlations were presented. In light of the spectral results, we propose to study the correlation by means of the spectral coherence γ between the flow field and the membrane deformation. To do so, the fluctuating signal $\tilde{y}'(t)$ of the membrane deformation at $\tilde{x} = 0$ and $\tilde{z}$ corresponding to the PIV plane (c.f. figure 1) is considered. The correlation is then performed with the fluctuating velocity at every point of the PIV field of view $\hat{u}'(\hat{x}, \hat{y}, t)$. The coherence as the normalized absolute value of the cross spectral density of these two quantities is obtained via:

$$\gamma_u(\hat{x}, \hat{y}, St) = \frac{\left|\mathcal{F}\left[\hat{u}'(\hat{x}, \hat{y}, t)\right] \mathcal{F}^\star\left[\tilde{y}'(t)\right]\right|^2}{E_{\hat{u}\hat{u}}(\hat{x}, \hat{y}, St) E_{\tilde{y}\tilde{y}}(St)}. \quad (1)$$

Here, $\mathcal{F}[\cdot]$ represents the fast Fourier transform, $|\cdot|$ represents the absolute value, the superscript $\star$ represents the complex conjugate and $E_{\hat{u}\hat{u}}$ and $E_{\tilde{y}\tilde{y}}$ are the power spectral density of the membrane deformation $\tilde{y}'$ or the velocity fluctuation $\hat{u}'$. Analogously, one computes γ_v by substituting $\hat{u}'$ with $\hat{v}'$. Note that, with this normalization, $0 \leq \gamma \leq 1$ where $\gamma = 0$ represents the total lack of coherence whilst a perfect coherence is given by $\gamma = 1$. A graphic summary of this procedure is found in figure 4. Given the practical difficulty of a three-dimensional representation of the function $\gamma_u(\hat{x}, \hat{y}, St)$, three two-dimensional cuts of the function at

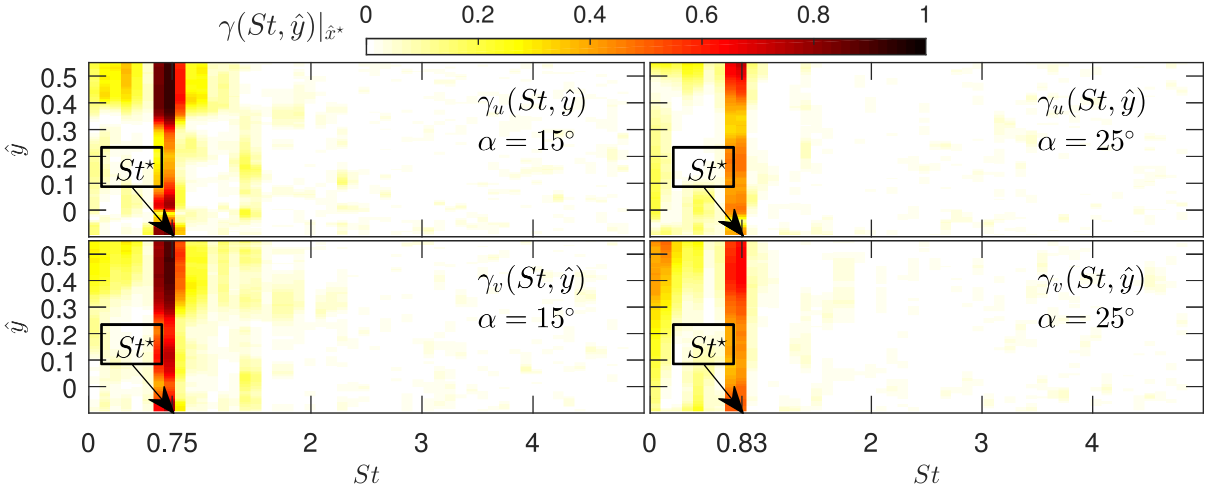

Figure 5: Coherence $\gamma(St, \hat{y})$ of the streamwise (top row) and vertical (bottom row) velocity fluctuations for the two angles of attack at $\hat{x} = \hat{x}^\star = 0.1$.

$\hat{x}^\star = 0.1$, $\hat{y}^\star = 0.4$ and $St^\star = 0.75$ are shown (the peak frequency at this location for the spectral content shown in figure 3).

Three main results can be observed in figure 4. (i) A significant coherence is maintained throughout the flow field except in those regions where, as suggested above, there exist clear shear layers. Moreover, $\gamma_u|_{St^\star}$ is close to zero in the region where these two shear layers merge, confirming the independence between the eddies in the shear layer and the membrane deformation. (ii) A second harmonic of $St^\star$ can be observed for $-1 < \hat{x} < 0$ at $\hat{y}^\star$. A third harmonic is significantly less evident and also appears for a much shorter streamwise extent. The appearance of these harmonics seem to be related with the point of maximum membrane deformation, perhaps due to the proximity to the wing. (iii) Downstream of the wing ($\hat{x}^\star = 0.1$) the second harmonic is negligible. Nevertheless, a significant level of coherence can be observed for every $\hat{y}$ (except at the points where the shear layers cross $\hat{x}^\star = 0.1$).

The difference between the two angles of attack and between γ_u and γ_v can be observed in figure 5. It is evident that the coherence is larger for the smaller angle of attack and the peak appears at different $St^\star$ (as shown above in figure 3). The differences between γ_u and γ_v are less evident, but the membrane deformation seem to be slightly more correlated with the vertical velocity. This was also shown by Bleischwitz et al. (2017) for the mean correlation.

To summarize, Bleischwitz et al. (2017) showed that there is a temporal correlation between the membrane deformation and the flow field. By means of spectral analysis the current study has been shown that there are two distinct regions of the flow: the wake of the wing and the shear layers separating this wake from the freestream. Furthermore, it has been demonstrated that the wing's wake is closely related with the membrane deformation as evidenced by the coherence between these two quantities at close to unity. This has important implications for the analysis of the flow-structure interaction of this phenomenon. In particular, the frequency relationship between flow and membrane is concentrated at a single frequency (within resolution); moreover, there is a linear relationship between them. These two facts suggest a suitability of low-order models to capture the flow-structure interaction around the membrane wings. The methodologies used will be briefly described in section 3 and the results will be presented in section 4.

3 Methodology

Various modes of the membrane deformation extracted by means of proper orthogonal decomposition (POD) were shown in Bleischwitz et al. (2016). Further, they linked these modes with the dominant eigenfunctions of the membrane vibration (by means of a sinusoidal decomposition). However, a link between a low-order model of the membrane and the flow was not presented. Given that there exists a clear relationship at a single frequency between the flow and the membrane deformation (as shown in section 2.2), a temporal-based modeling approach would intuitively seem most suitable. As a basis, the most energetic POD modes capture structures without considering how one flow instance maps into the next, and instead treating the flow as an ensemble that can be reassembled through a set of coefficients. In contrast, tools such as the Dynamic mode decomposition (Schmid, 2010) associate particular spatial structures with a distinct frequency such that modes are orthogonal in time (i.e. they shrink or grow at distinct characteristic frequencies). Below we introduce the nomenclature that will be employed and describe briefly various low-order DMD-based modeling techniques.

The notation $\boldsymbol{v}_k \in \mathbb{R}^J$ for the k-th snapshot for $k = 1, 2, \ldots, K = 5000$ is used. Here J is twice the number of spatial data points as the data was acquired by means of two-dimensional PIV. The number of spatial points changes slightly in the two considered cases due to reflection of light in the membrane and the angle of attack but is approximately $J_{PIV} \approx 6 \times 10^4$. The snapshots are arranged as the columns of a matrix $V_1^K = [\boldsymbol{v}_1, \boldsymbol{v}_2, \ldots, \boldsymbol{v}_K]$ and the notation for a subset of consecutive snapshots is given as $A \leq k \leq B$: $V_A^B = [\boldsymbol{v}_A, \boldsymbol{v}_{A+1}, \ldots, \boldsymbol{v}_{B-1}, \boldsymbol{v}_B]$. Of particular advantage in using DMD is its completely general application, i.e. the method's ignorance to underlying physical phenomena. As a consequence of this flexibility the implementation for both flow and membrane is identical, where the membrane deformations are similarly formatted into columns and ordered sequentially (the only marginal difference being in the total number of degrees of freedom $J_{DIC} \approx 10^4$).

In general, a low order representation such as the ones outlined below seeks two elements. First, a suitable linear subspace P, such that, by projecting onto it, the degrees of freedom are significantly reduced from J in the real space to some $N \ll J$ in the projected space. Following the projection, the dynamics of the flow are modelled as a linear evolution of N eigenvectors with N associated frequencies and damping coefficients.

The four methods presented offer distinct methodologies to calculate the projection subspace as well as the linear dynamics. To start, the traditional dynamic mode decomposition (Schmid, 2010) is described in section 3.1. Three variants that have since emerged from DMD will be subsequently presented: optimal mode decomposition (OMD; Wynn et al., 2013) in section 3.2; total-least-squares based dynamic mode decomposition (DMDtls; Dawson et al., 2016) in section 3.3 and high-order dynamic mode decomposition (DMDho; Le Clainche and Vega, 2017) in section 3.4. Once the projection subspace and the linear dynamics are obtained using any of the four methods, some further considerations common to all of them are summarized in section 3.5.

Henceforth, the superscript T will represent the transpose of a matrix. The operator $\mathrm{diag}(\cdot)$ applied to a matrix will provide a vector whose elements are the diagonal of the matrix. Analogously, the same operator applied to a vector will generate a diagonal matrix with the elements of the vector along the diagonal. The operator $||\cdot||_F^2$ will represent the second order Frobenius norm of a matrix. Unless otherwise stated, SVD will represent the economy-sized singular value decomposition of a matrix.

3.1 Dynamic mode decomposition (DMD)

First developed by Schmid (2010), the central idea behind DMD is to model a particular snapshot as a linear evolution from the previous one, mathematically: $\boldsymbol{v}_{k+1} \approx R\boldsymbol{v}_k$. In matrix form:

$$V_2^K \approx R V_1^{K-1}, \tag{2}$$

where $R \in \mathbb{R}^{J \times J}$. In order to solve for R one considers the POD decomposition (obtained by SVD) of the snapshots such that

$$V_1^{K-1} = W \Sigma T^T, \tag{3}$$

where W is a matrix of orthogonal spatial modes, Σ a matrix containing the singular values, and T^T the orthogonal temporal basis. Furthermore, it may be desirable to truncate a number of POD modes which may be dominated by experimental noise and keep only those N modes whose energy (proportional to the singular values) is larger than a certain threshold $\sigma_{N+1}/\sigma_1 < \epsilon_t$ where the energies $\boldsymbol{\sigma} \equiv [\ldots, \sigma_i, \ldots] = \mathrm{diag}(\Sigma)$ are placed in decreasing order. Following the truncation, the POD results in $V_1^{K-1} \approx \hat{W}\hat{\Sigma}\hat{T}^T$ where $\hat{W}^T\hat{W} = I_N$ is the identity matrix of size $N \times N$ and the hat symbol denotes the reduced POD space. Projecting equation (2) in the truncated POD modes (i.e. premultiplying by $\hat{W}^T$) and reordering one obtains

$$\hat{R} = \hat{W}^T V_2^K \hat{T} \hat{\Sigma}^{-1}, \tag{4}$$

where $\hat{R} = \hat{W}^T R \hat{W}$ is the projection of the DMD matrix, R, into the reduced POD space.

3.2 Optimal mode decomposition (OMD)

As described in Wynn et al. (2013), the OMD algorithm can be observed as a modification of the basic DMD procedure. Whilst the POD projection given in equation (3) is exact; its truncated counterpart ($V_1^{K-1} \approx \hat{W}\hat{\Sigma}\hat{T}^T$) is no longer so. Therefore, there may exist a certain linear subspace such that the projection onto it provides a smaller error than in the truncated POD space $\hat{W}$. In other words, while DMD minimizes $||V_2^K - \hat{W}^T\hat{R}\hat{W}V_1^{K-1}||_F^2$; OMD will seek the matrices L and $\hat{R}$ such that $||V_2^K - L\hat{R}L^T V_1^{K-1}||_F^2$ is minimum subject to $LL^T = I_N$ (for a user-prescribed projection rank N). It can be shown that for a given L the matrix $\hat{R}$ that minimizes the error is given by

$$\hat{R} = L^T V_2^K V_1^{K-1} L (L^T V_1^{K-1} (V_1^{K-1})^T L)^{-1}. \tag{5}$$

The problem is therefore reduced to the search of a suitable subspace L of rank N which minimizes the Frobenius norm of the residual. For more details about the numerical strategy the reader is referred to Wynn et al. (2013).

Although the rank of the projection subspace can be prescribed a priori, for consistency, the same N as that in the DMD algorithm based on the energy of the POD modes is used in the present study. $\hat{W}$ is also employed as initial condition for the numerical search of L.

3.3 Total least squares dynamic mode decomposition (DMDtls)

The DMDtls approach of Dawson et al. (2016) maintains the projection onto the POD space. However, it modifies the way $\hat{R}$ is computed in order to account for experimental noise. It is assumed that $\boldsymbol{v}_{k+1} \approx R\boldsymbol{v}_k$ is equivalent to minimizing the residual $\boldsymbol{e}_{k+1}$ in $\boldsymbol{v}_{k+1} + \boldsymbol{e}_{k+1} = R\boldsymbol{v}_k$ through the process described in section 3.1. However, this implies that no residual is present in the snapshot $\boldsymbol{v}_k$. Dawson et al. (2016) proposed to consider both residuals $\boldsymbol{v}_{k+1} + \boldsymbol{e}_{k+1} = R(\boldsymbol{v}_k + \boldsymbol{e}_k)$ and find the R that minimizes both of them simultaneously. By projecting this expression onto the first N POD modes (given by $\hat{W}$) and reordering

$$\begin{bmatrix}\hat{R} - I_N\end{bmatrix} \begin{bmatrix}\hat{V}_1^{K-1} + \hat{E}_1 \\ \hat{V}_2^K + \hat{E}_2\end{bmatrix} = 0\,, \tag{6}$$

where the matrices $\hat{E}_1 = [\hat{\boldsymbol{e}}_1, \ldots, \hat{\boldsymbol{e}}_{K-1}]$ and $\hat{E}_2 = [\hat{\boldsymbol{e}}_2, \ldots, \hat{\boldsymbol{e}}_K]$ are obtained by projecting the residual vectors $\boldsymbol{e}_k$ $(k = 1, \ldots, K)$. One can also define $E = \begin{bmatrix}\hat{E}_1 \\ \hat{E}_2\end{bmatrix}$ as the residual matrix. Note that, although this algorithm is valid for any $2N < K$, for consistency with the other methods present the first N POD modes are used in the present study as described in section 3.1.

The SVD decomposition $\begin{bmatrix}\hat{V}_1^{K-1} \\ \hat{V}_2^K\end{bmatrix} = USH^T$ is then considered (with analogous notation to equation (3)). In general, S will be full rank ($2N$) due to sensor noise. This is clearly at odds with the first matrix of equation (6) whose maximum rank is N. The minimization of the residual $||\hat{E}||_F^2$ is performed by approximating S with the closest N-ranked matrix. According to the theorem presented in Eckart and Young (1936), this is possible if the first N elements of $\boldsymbol{s} = \mathrm{diag}(S)$ are maintained and set $s_i = 0$ for $N + 1 \leq i \leq 2N$:

$$\min||E||_F^2 \;\Leftrightarrow\; \begin{bmatrix}\hat{V}_1^{K-1} \\ \hat{V}_2^K\end{bmatrix} \approx \begin{bmatrix}U_{11} & U_{12} \\ U_{21} & U_{22}\end{bmatrix} \begin{bmatrix}S_{11} & 0 \\ 0 & 0\end{bmatrix} \begin{bmatrix}H_1^T \\ H_2^T\end{bmatrix} = \begin{bmatrix}U_{11}S_{11}H_1^T \\ U_{21}S_{11}H_1^T\end{bmatrix}\,. \tag{7}$$

This expression can therefore substitute the second matrix in equation (6) resulting in $\hat{R} = U_{21}U_{11}^{-1}$.

3.4 High order dynamic mode decomposition (DMDho)

One interpretation of DMDtls is that it is a modification of DMD which takes information from snapshots both before and after to form the matrix $\hat{R}$. Similarly, Le Clainche and Vega (2017) proposed a higher order expansion of equation 2 in which a snapshot is estimated as a linear combination of the previous d snapshots:

$$\boldsymbol{v}_{k+d} \approx R_1\boldsymbol{v}_k + R_2\boldsymbol{v}_{k+1} + \cdots + R_d\boldsymbol{v}_{k+d-1}\,. \tag{8}$$

Projecting onto the first N POD modes (as done in sections 3.1 and 3.3) and rearranging equation (8) in matrix form $\tilde{V}_2^{k-d+1} = \tilde{R}\tilde{V}_1^{k-d}$ is obtained where

$$\tilde{R} = \begin{bmatrix} 0 & I & 0 & \cdots & 0 & 0 \\ 0 & 0 & I & \ddots & 0 & 0 \\ \vdots & \ddots & \ddots & \ddots & \ddots & \vdots \\ 0 & 0 & 0 & \ddots & I & 0 \\ \hat{R}_1 & \hat{R}_2 & \hat{R}_3 & \cdots & \hat{R}_{d-1} & \hat{R}_d \end{bmatrix} \text{ and } \tilde{V}_1^{k-d+1} = \begin{bmatrix} \hat{V}_1^{k-d+1} \\ \hat{V}_2^{k-d+2} \\ \vdots \\ \hat{V}_{d-1}^{k-1}\hat{V}_d^k \end{bmatrix}\,. \tag{9}$$

A second model reduction is then performed by considering the SVD $\tilde{V}_1^{k-d+1} = USV^T$ to be truncated at N' modes such that $s_{N'+1}/s_1 \leq \epsilon_t$ with $s_i = \mathrm{diag}(S)$: $\tilde{V}_1^{k-1+1} \approx \tilde{U}\tilde{S}\tilde{V}^T$. Projecting $\tilde{V}_2^{k-d+1} = \tilde{R}\tilde{V}_1^{k-d}$ onto the truncated SVD modes $\tilde{U}$ results in $T_2^{k-d+1} = \bar{R}T_1^{k-d}$ where $\bar{R} = \tilde{U}^T\tilde{R}\tilde{U}$ and $T_1^{k-d+1} = \tilde{S}\tilde{V}^T$. This is solved for $\bar{R}$ by pseudo-inverting the SVD of $T_1^{k-d} = A\Lambda B^T$: $\bar{R} = T_2^{k-d+1}B\Lambda^{-1}A^T$.

3.5 Reconstruction considerations

For convenience, the various projection subspaces are referred to as P where $P^TP = I_N$ and $P = \hat{W}$ for DMD, DMDtls and DMDho or $P = L^T$ for OMD. In the four cases, the linear dynamics are given by $\hat{R}$. First, the original snapshots are projected onto the subspace P as: $\hat{V}_1^K = [\hat{\boldsymbol{v}}_1, \ldots, \hat{\boldsymbol{v}}_K] = PV_1^K$. To extract the dynamics, the eigenvectors[1] $\boldsymbol{q}_i \in \mathbb{C}^N$ and eigenvalues μ_i $(i = 1, \dots, N)$ of $\hat{R}$ are computed and the snapshots are reconstructed using:

$$\hat{\boldsymbol{v}}_k \approx \sum_{i=1}^{N} a_i \boldsymbol{q}_i \mu_i^{k-1} \ , \ k = 1, 2, \dots, K \, . \tag{10}$$

The unknown amplitudes a_i correspond to the projection of the first snapshot onto the i-th mode. In practice, they are obtained by a least squares fitting. To do so the eigenvalues and eigenvectors are arranged into matrices such that $Q = [\boldsymbol{q}_1, \dots, \boldsymbol{q}_N] \in \mathbb{C}^{N \times N}$ and $M = \mathrm{diag}(\mu_i) \in \mathbb{C}^{N \times N}$. As such, following (10), K equations are written as $L\boldsymbol{a} = \boldsymbol{b}$ (see e.g. Le Clainche and Vega, 2017) where

$$L = \begin{bmatrix} Q \\ QM \\ QM^2 \\ \vdots \\ QM^{k-1} \end{bmatrix} \ , \ \boldsymbol{a} = \begin{bmatrix} a_1 \\ a_2 \\ \vdots \\ a_N \end{bmatrix} \ \text{and} \ \boldsymbol{b} = \begin{bmatrix} \hat{\boldsymbol{v}}_1 \\ \hat{\boldsymbol{v}}_2 \\ \vdots \\ \hat{\boldsymbol{v}}_K \end{bmatrix} \, . \tag{11}$$

The amplitudes are obtained by solving the system $L\boldsymbol{a} = \boldsymbol{b}$ through pseudo-inverting the matrix L. The modes in the real space are defined as $\boldsymbol{\phi}_i = P\boldsymbol{q}_i$ $(\Phi = [\boldsymbol{\phi}_1, \boldsymbol{\phi}_2, \dots, \boldsymbol{\phi}_N] = PQ$ in matrix form). The characteristic damping coefficients $\delta_i = \mathrm{Re}(\log(\mu_i))/\Delta t$ and frequencies $\omega_i = \mathrm{Im}(\log(\mu_i))/\Delta t$ of the linear evolution are given by the complex eigenvalues of the matrix $\hat{R}$ and are the same in the real and projected spaces.

With the dynamic modes, amplitudes, and eigenvalues obtained the low-order reconstruction of the original snapshots $\boldsymbol{v}_k$ is performed as:

$$\boldsymbol{v}_k \approx \boldsymbol{v}_{k,rec} = \sum_{i=1}^{N} a_i \boldsymbol{\phi}_i e^{(\delta_i + i\omega_i)\Delta t(k-1)} \ , \ k = 1, 2, \dots, K \, . \tag{12}$$

3.6 Selection of parameters

The DMD-based methods start by maintaining only the N most energetic POD modes such that $\sigma_{N+1}/\sigma_1 < \epsilon_t$. The parameter ϵ_t is prescribed by the user and should be similar to the uncertainty in the velocity (or membrane deformation) measurements (Le Clainche et al., 2017). The larger the value of chosen ϵ_t, the more POD modes that are discarded as noise. In the present case, different values of ϵ_t were tested from 0.01 to 0.05. Whilst the former may be too optimistic, particularly for membrane deformation measurements (Bleischwitz et al., 2017), it is reasonable to assume that the uncertainty in the measurements was lower than 5%. After some preliminary tests (not shown for brevity) it was found that $\epsilon_t = 0.02$ provided the best compromise between capturing the essential dynamics of the flow whilst keeping the number of noisy modes to a minimum. Note that this value must be chosen for a given experiment. Nevertheless, the results did not present major qualitative changes for other values of ϵ_t.

In the DMDho algorithm, d has to be specified *a priori*. As discussed in Le Clainche and Vega (2017) and Le Clainche et al. (2017) it should be comprised between $d \gg 1$ and a maximum number which scales with $d \sim K/3$. Different values of $100 \leq d \leq 1000$ were tested with little influence in the results. Nevertheless, a slightly better performance (in terms of the residual between the reconstructed and original fields) was achieved with $d = 300$ hence that value will be used throughout the present study.

4 Results

4.1 Flow description: frequencies, dampings, amplitudes and modes

Low-order models such as the those in the present study are utilized based on their ability to detect dynamics present within the flow. The temporal characteristics of these dynamics are described by their frequency and damping (growth or decay) given by the imaginary and real parts respectively of the eigenvalues of the reduced dynamic matrix $\hat{R}$. Similarly, their spatial structure is described by the modes ϕ. Note that, for multi-component data such as the present PIV, each mode $\phi_i \in \mathbb{C}^J$ can be divided in stream-wise and stream-normal modes ϕ_i^u and ϕ_i^v respectively. As all of the data considered is real, the modes appear either as real modes (associated with null frequencies) or in pairs of complex conjugates. Nevertheless, the modes' shape is independent of any normalization. For simplicity, each pair of conjugate modes will be referred to as a single mode thereafter. The modal amplitude a_i (calculated as described in section 3.5) is proportional to the importance of the i-th mode in the flow reconstruction.

[1] In the DMDho case, it is necessary to first compute $\bar{\boldsymbol{q}}_i$, the eigenvalues of $\bar{R}$. The eigenvectors $\boldsymbol{q}_i$ are then obtained by retaining only the first N components of $\tilde{U}\bar{\boldsymbol{q}}$.

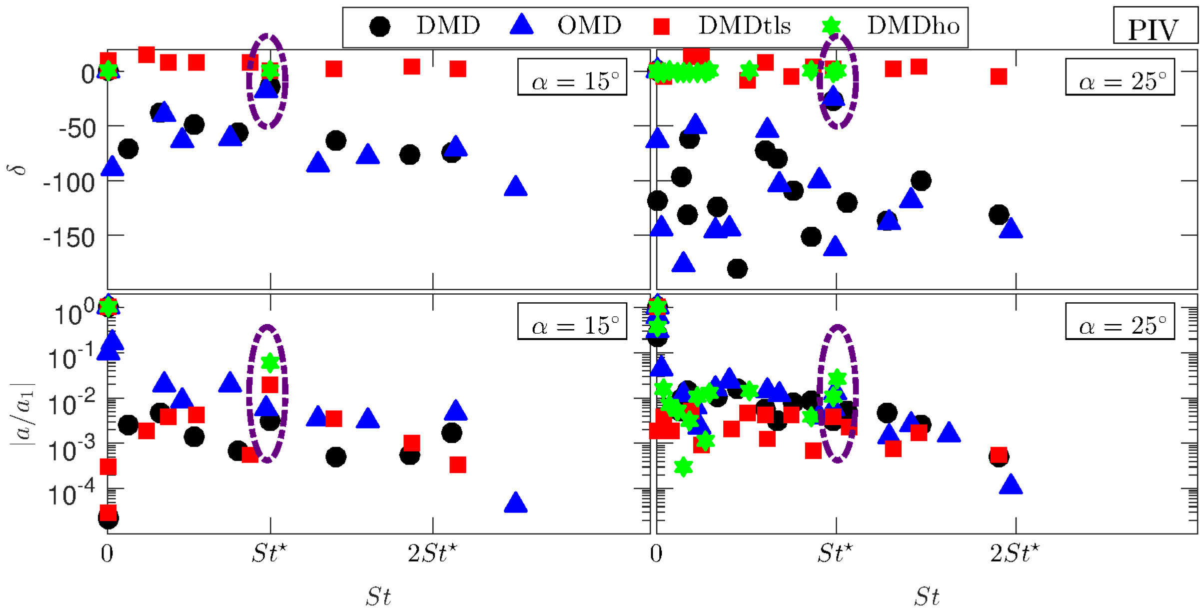

Figure 6: Damping coefficient δ, and amplitude a as a function of the frequency St for various decomposition methods of the flow field (PIV) data at the two angles of attack.

Figure 6 presents the modal damping and amplitudes for the various methods at both angles of attack. Frequencies and modes are calculated in complex conjugate pairs but, for brevity, only the positive part of the spectra is shown. Spectral measurements indicate that a quasi-periodic motion is expected in most of the flow field (c.f. figure 3). One would therefore expect the modal damping to be zero corresponding to a steady periodic motion. It is strikingly clear, however, that this is not the case for DMD and OMD cases. Substituting $\delta \approx -50$ in equation (12) implies that after a few snapshots ($k \approx 500$) the mode's gain is already $e^{-50\Delta t k} \approx 10^{-14}$. The reconstructed signal therefore vanishes after a few snapshots and these modes cannot describe the physics of the flow. This was previously reported by Dawson et al. (2016) for noise-contaminated measurements who, using synthetic data, showed that truncated DMD and OMD algorithms are unable to capture accurately the value of the mode damping. Similarly, Bagheri (2014) related process noise with a parabolic decay in the estimated damping coefficients. It is expected that the present measurements present both measurement noise (due to the experimental uncertainty) and process noise (due to the non-linearity of the underlying turbulent flow). Thus it is not surprising that the damping coefficients are inaccurately estimated. This has further implications on the amplitudes determined by means of equation (10). The methodology finds a_i such that they minimize the least square error between the reconstructed and the original snapshots. However, if the reconstructed snapshots are virtually zero after a few time steps the interpretation of a_i is rendered invalid.

In order to minimize the influence of signal noise, Dawson et al. (2016) proposed to use DMDtls as a means to obtain the low-order dynamics $\hat{R}$ as described in section 3.3. Figure 6 shows that the damping coefficients using DMDtls are significantly closer to $\delta \approx 0$. From a qualitative point of view, this reflects the underlying flow more accurately; approaching the condition of steady periodicity. Nevertheless, from a quantitative point of view, these damping coefficients are also problematic. In fact, some of them are even $\delta_i > 0$; implying that $e^{\delta_i \Delta t k} \to \infty$. This necessarily implies that $a_i \to 0$ for those modes with $\delta_i > 0$ (as the data is finite).

Some of these problems may be solved by using DMDho as described in section 3.4. By including a larger number of previous snapshots, the damping and frequencies of the flow are estimated with more accuracy due to the method receiving information of a larger time interval to estimate a given snapshot (c.f. equation (8)). In this case, the number of modes is largely reduced as the POD modes are truncated twice hence only the most important modes survive the double truncation. In contrast with the previous methods, the damping coefficients estimated by means of DMDho are virtually 0 as would be expected for steady periodic motion. They are not strictly 0 due to numerical and experimental noise however their small magnitude implies negligible amplification or damping across the 5000 snapshots.

A further challenge when interpreting the results of these low-order models is identifying the representative dynamics. Following the spectral results of figure 3, one would expect that the flow may be largely described by a single mode/frequency pair whose spatial and temporal properties provide a qualitative description of the flow. The selection of a single mode is straightforward in the DMDho case for $\alpha = 15^\circ$ where the double truncation removes all the modes but two; one associated with the mean flow and another one at a frequency similar to the Fourier spectra. However, this is not so straightforward in the other cases. Ideally the modes

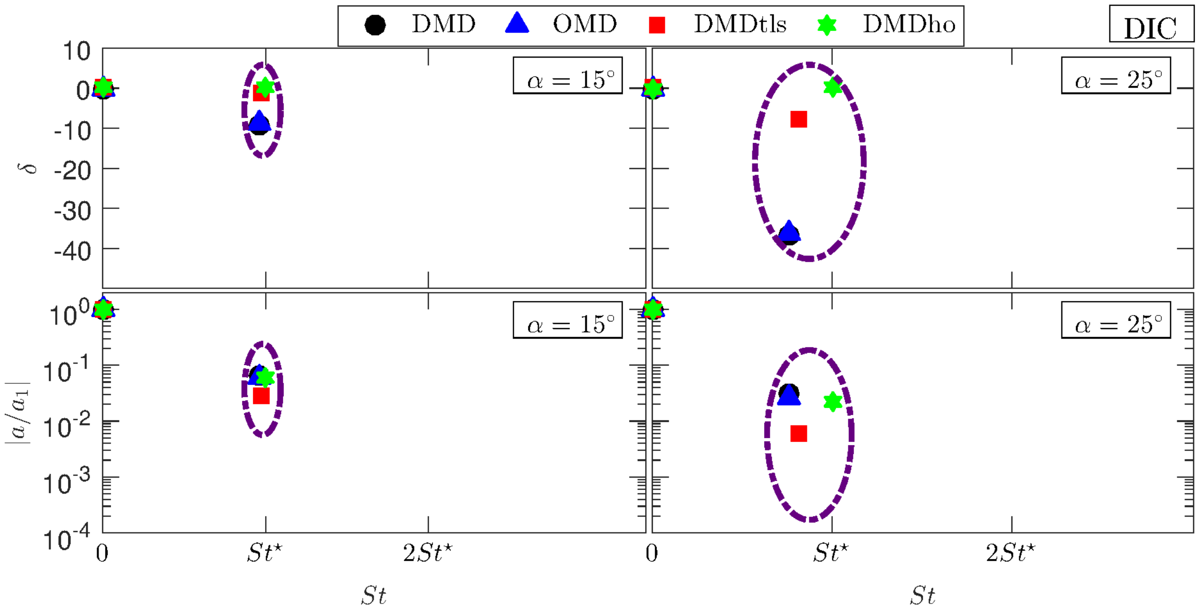

Figure 7: Damping coefficient δ, and amplitude a as a function of the frequency St for various decomposition methods of the membrane deformation (DIC) data at the two angles of attack.

would be selected by assessing the decompositions' results without resorting to known information such as the spectral content of the flow. For flows with apparent periodic motion one could make an argument to select those modes with their damping as close to 0. Nevertheless it seems ill-posed given that the damping coefficients are easily incorrectly estimated. This is also problematic when assessing results from DMDtls or DMDho since the damping coefficients are virtually 0. In those cases, the most reasonable assumption is to select the modes with the second highest amplitude a_i (in convective flows the largest amplitude is always associated with the mean flow). The problem exists however that large a_i may be artificially associated with highly damped modes; pointing to a connection between the wrongly estimated damping coefficients and the modes' amplitudes. To avoid this problem Thomareis and Papadakis (2017) proposed using $|a_i e^{\delta_i \Delta t K}|$ as mode-selection criteria for their application of non-truncated DMD of the direct numerical simulation of flow around an airfoil. However, in our current dataset $e^{\delta \Delta t K}$ vanishes independently of how large is a_i.

In summary, the damping coefficients are not correctly estimated; implying that mode selection based on δ_i is problematic. Analogously, it implies that the values of a_i are somehow contaminated by the wrong estimation of δ_i hence any possible mode selection based on a_i may also be ill-advised. The method in which these two problems are absent is DMDho where the damping coefficients are virtually 0 hence the information contained in a_i is more meaningful.

The same methods can be applied to the membrane deformation data to obtain the characteristic frequencies and damping coefficients. The results of this decomposition are presented in figure 7 along with the modes' amplitudes. Unlike the turbulent flow in the wing's wake, the membrane deformation can be more closely approximated by a linear process. Consequently, the various methods only detect two significant modes which resemble the mean deformation and the primary vibrational mode. This could be anticipated given the POD decomposition presented in Bleischwitz et al. (2016) where the first fluctuating mode contains 84.3% of the energy for the $\alpha = 15^\circ$ case. Nevertheless, the problem of inaccurate estimation of the damping coefficients is still present for the truncated DMD and OMD methods.

Despite the difficulty in selecting a single mode/frequency pair for the flow data the modes with either smallest damping (for DMD and OMD methods) or with largest amplitude (for DMDtls and DMDho) are tentatively selected. The selected modes are encircled with a dashed line in figures 6 and 7 and their properties ($|a^\star/a_1|$, $St^\star$ and $\delta^\star$) summarized in table 1. From a qualitative perspective, it is clear that all the four methods capture the same flow event characterized by $St \approx 0.75$ or $St \approx 0.83$ for the $\alpha = 15^\circ$ and $\alpha = 25^\circ$ cases respectively. In the present case the frequency resolution is $\Delta f = 0.8\,\mathrm{Hz}$ which, in non-dimensional units, corresponds to $\Delta St \approx 0.01$. Consequently, the dispersion obtained in $St^\star$ is of the same order of that of the Fourier spectra. From a qualitative point of view, the relative difference between the characteristic frequency of the flow and membrane deformation (shown in the last row of table 1) is reasonable for all the four methods for $\alpha = 15^\circ$. Nevertheless, it is clear that the DMDho performance is at least two orders of magnitude better at estimating the same frequency for both flow and membrane deformation. In fact, if one only considers DMD, OMD and DMDtls methods for the $\alpha = 25^\circ$ case; one could conclude that there is not any significant flow-

		$\alpha = 15°$				$\alpha = 25°$			
		DMD	OMD	DMDtls	DMDho	DMD	OMD	DMDtls	DMDho
PIV	Number of modes	20	20	20	3	33	33	33	26
	$\lvert a^\star/a_1 \rvert$(%)	12	0.029	0	5.9	6.0	9.0	8.2	2.4
	$St^\star$	0.747	0.731	0.748	0.750	0.820	0.827	0.817	0.836
	$\delta^\star$	-14	-17	0.066	0.013	-27	-160	2.7	-0.027
DIC	Number of modes	3	3	3	3	3	3	3	3
	$\lvert a^\star/a_1 \rvert$ (%)	6.6	5.8	2.8	5.9	3.2	2.5	0.59	2.2
	$St^\star$	0.724	0.724	0.735	0.750	0.628	0.629	0.675	0.836
	$\delta^\star$	-9.2	-8.9	-1.5	0.0061	-37	-36	-7.9	0.044
	$\frac{St^\star_{PIV}-St^\star_{DIC}}{St^\star_{DIC}}$ (%)	3.1	0.90	1.7	0.0033	23	24	17	0.061

Table 1: Summary of frequencies, damping coefficients and amplitudes for the decompositions of PIV and DIC data for the selected modes. Lower row shows the relative difference between the estimated frequencies of the flow and membrane deformation. Note that 3 modes correspond with a mode for the mean flow plus a pair of conjugate modes hence representing a single dynamic phenomenon.

structure interaction as the characteristic frequencies are significantly different (up to 24% difference). However, the same phenomena studied by means of DMDho shows virtually no difference between the PIV and membrane frequencies implying a significant flow-structure interaction as was reported by Bleischwitz et al. (2017).

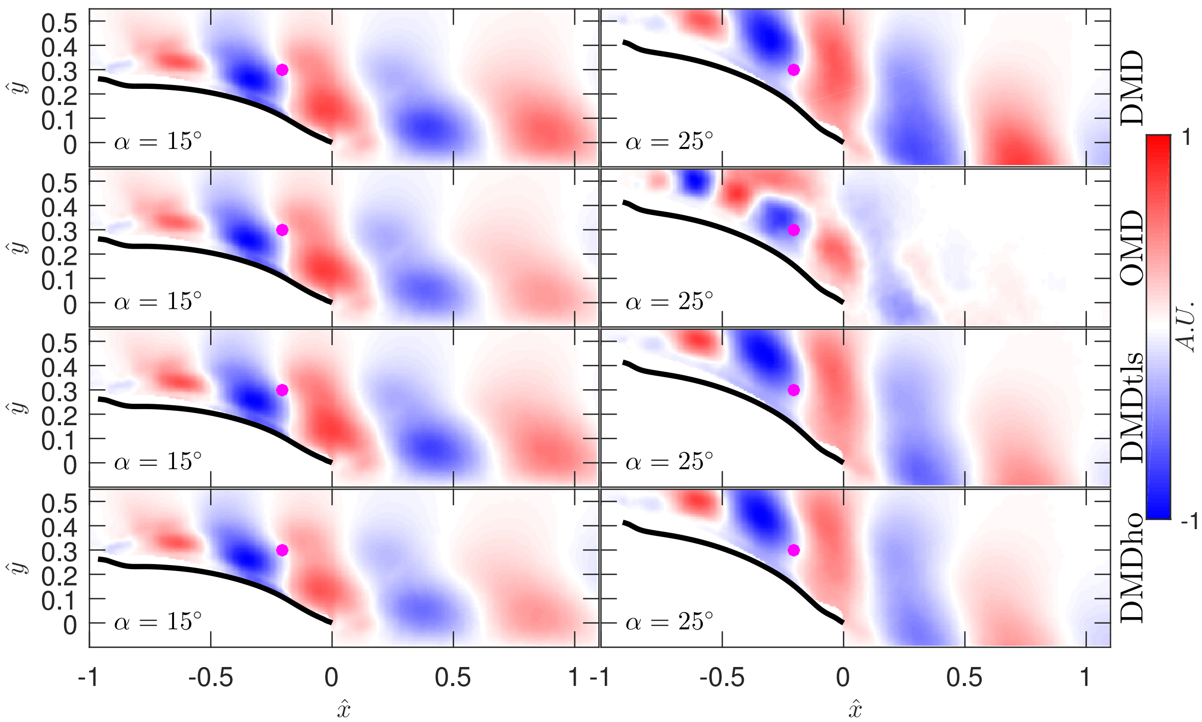

Figure 8: Real part of the characteristic flow mode $\phi^v_\star$ (at frequency $St^\star$) for various decomposition and the two angles of attack. The modes are arbitrarily normalized such that the imaginary part of $\phi^v_\star$ at the location of the pink dot ($\hat{x} = -0.2$, $\hat{y} = 0.3$) is null.

Apart from the temporal properties (damping and frequencies) it is also of interest to inspect the spatial structure of the modes for the various decompositions. Figure 8 shows the the vertical mode $\phi^v_\star$ associated with the frequencies summarized in table 1 and encircled in figure 6. The modes' normalization is arbitrary and their real part changes according to the normalization coefficient. Thus, in order to present a meaningful comparison, the modes are normalized such that the imaginary part of $\phi^v_\star$ at the point $\hat{x} = -0.2$, $\hat{y} = 0.3$ is null. Then their real part is plotted in figure 8 for the various methods and angles of attack. It is clear that, despite small differences, the spatial structure of the modes remains independent of the decomposition method. The largest difference is observed for the OMD decomposition of the $\alpha = 25°$ case. This is not surprising as OMD is the only method that seeks an alternative low-order subspace to project the dynamics.

The dominant mode shape is related with the leading edge vortex rolling and convecting downstream along the membrane chord. The reminiscence of this vortex is also observed for $\hat{x} > 0$ i.e. downstream of the trailing edge. This mode shape is in agreement with the observations of the most energetic POD mode of the velocity fluctuations presented in Bleischwitz et al. (2017). In fact, the mode/frequency pair establishes an straightforward relationship between the spectral content shown in figure 3 and the formation of leading edge vortices.

To summarize, any of the four tested methods are able to provide a qualitative description of the flow. This implies that the frequencies and mode shapes found by any of these methods are relatively insensitive to the methodology. However, the damping coefficients (and therefore the amplitudes) are not correctly estimated except for the DMDho method. This may imply important qualitative differences when assessing the fluid-structure interaction (which has been reported to be significant indeed using the spectral coherence figure 5). The selection of the dominant mode/frequency pair is also observed to be challenging for methods other than DMDho due to the problem with the damping estimation. A more demanding assessment can be performed by assessing the flow reconstruction using equation 12 as will be investigated in the following section.

4.2 Flow reconstruction

Section 4.1 discussed which are the most dominant modes and frequencies of the flow field and the membrane deformation. Here, the flow/membrane reconstruction is focused. As described above, the flow can be reconstructed using a linear combination of spatial modes evolving temporally with characteristic frequency and damping (c.f. equation 12).

4.2.1 Reconstruction via calculated damping coefficients

As a first approach, the time series at an arbitrary point located in the wing's wake ($\hat{x} = -0.2$, $\hat{y} = 0.3$ shown with a pink dot in figure 8) is studied. Due to it's relation to the membrane deformation, in the following the analysis is focused around the fluctuations of the vertical flow velocity normalized with the freestream velocity $\hat{v}' = v'/U_\infty$. Figure 9 shows the measured velocity compared with its reconstructed counterpart using the various methodologies. Three subsets are zoomed in on to highlight distinct distinct aspects of the results.

For times $\hat{t} < 10$ all of the decompositions perform adequately. However, by $\hat{t} \sim 10$ the estimations using DMD and OMD vanish to 0. This was previously discussed in section 4.1 as a consequence of the incorrect estimation of the damping coefficient. This problem is more significant for the OMD method (also reported by Baj et al., 2015; Rodríguez-López et al., 2016) which vanishes for $\hat{t} \sim 1$. The reconstruction based on DMDtls slowly grows in amplitude until $\hat{t} \sim 230$ where the exponential term $e^{\delta \Delta t k}$ tends to infinity and so the reconstructed velocity. For large times $\hat{t} > 400$ the only signal which is not either 0 or infinity is the reconstruction based on DMDho. This reflects the properties mentioned above: first, DMDho estimates the damping coefficients more adequately. Despite the fact that they are not strictly 0 (c.f. table 1) their influence up to $\hat{t} \sim 500$ is negligible as observed in figure 9. In addition, the frequency estimation is reasonable. This can be observed qualitatively in the top right subplot of figure 9 where the sinusoidal line estimated by DMDho appears to align with the peaks of the velocity fluctuation measured with PIV.

4.2.2 Reconstruction via artificially null damping coefficients

The main barrier to a good reconstruction seems to be the incorrect determination of the damping coefficients either due to noise contamination or due to the inability of the various methods to capture the underlying non-linear dynamics over long times. The non-zero estimation of these damping coefficients result in reconstructed velocities that either vanish or tend to infinity. Given that the present flow is expected to be quasi periodic, it is of interest to have the damping coefficients artificially set to $\delta_i = 0$ and then the flow field reconstructed using equation (12). This provides a useful comparison using the same analysis of the velocity time series shown in figure 10.

In contrast to tha results in figure 9, the reconstructed velocity neither vanishes nor tends to infinity in figure 10 by design. Note that as the damping for the DMDho was already near zero the result is virtually unaltered. For the other decompositions, the magnitude is significantly smaller than the reconstructed velocity field. This may not pose a problem for some applications like flow control but compromises undoubtedly the flow reconstruction. This is further evidenced by the sinusoids following less closely the velocity signal measured by means of PIV. This frequency mismatch is particularly clear in the OMD case dominated by an artificial low-frequency component.

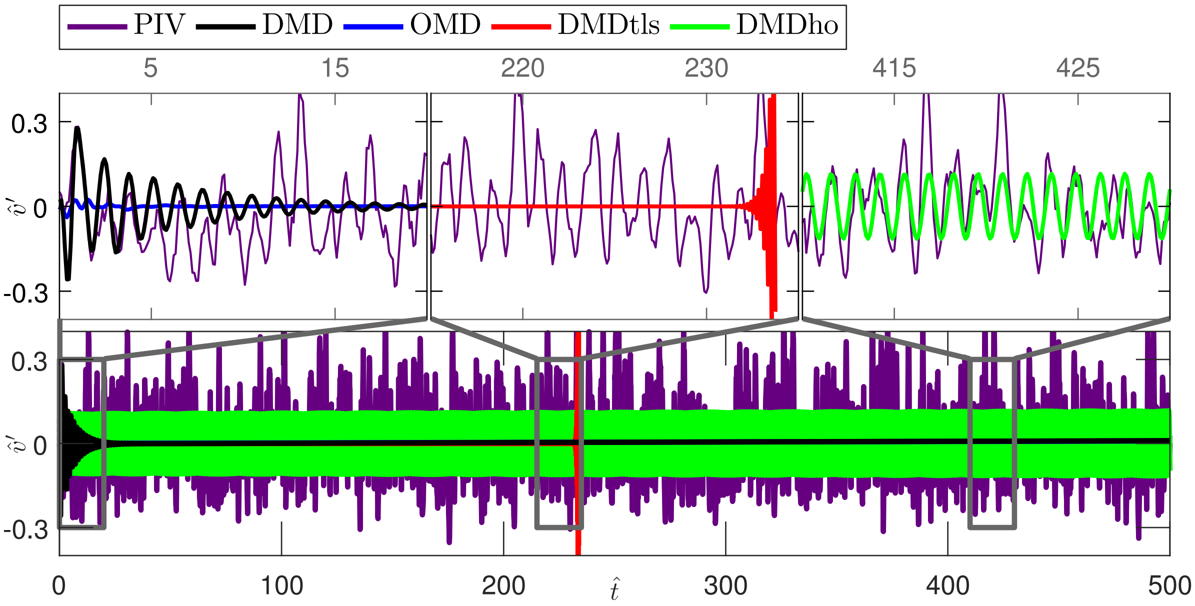

Figure 9: Normalized vertical velocity fluctuations $\hat{v}'$ at an arbitrary point ($\hat{x} = -0.2$, $\hat{y} = 0.3$, shown with a pink dot in figure 8) measured by PIV and using the various decomositions. The three upper plots represent zoomed regions of the lower graph. For clarity, some lines are suppressed in these zoomed plots.

4.2.3 Correlations of reconstructions with original flow field

One way to quantify the phase alignment between the signals of the original and reconstruction is to define the temporal correlation coefficient ρ as

$$\rho_u(\hat{x}, \hat{y}) = \frac{\overline{u'(\hat{x}, \hat{y}, \hat{t}) u'_{rec}(\hat{x}, \hat{y}, \hat{t})}}{u'_{rms} u'_{rec,rms}}, \tag{13}$$

where the overline represents the temporal average. Similarly, ρ_v is defined by substituting the stream-wise velocity u' by the vertical velocity v'. A perfect correlation $\rho = 1$ only implies that, at every instant of time, the undulations of the signals are in phase. This is judged to be sufficient to quantify the degree of the reconstruction of the velocity fields. However this criterion neglects the significantly lower magnitude of $\hat{v}'$ shown in figure 10. The overall performance of each method is assessed by considering the spatial average over the J points considered in the decompositions: $\langle \rho_u \rangle$ or $\langle \rho_v \rangle$. Analogously, for the membrane deformation $\tilde{y}$ and $\tilde{y}_{rec}$ and their correlation coefficient $\rho_y(\tilde{x}, \tilde{z})$ (with spatial average $\langle \rho_y \rangle$). To avoid to the issue of vanishing or infinitely large velocities, the correlations are presented for the artificially null damping coefficients $\delta = 0$ reconstructions.

Figure 11 shows the correlation map for the vertical velocity fields. The correlation is always higher for the $\alpha = 15°$ case than for the $\alpha = 25°$ case. This is probably due to the periodic shedding from the leading edge for the former for which the wake is less dominated by the chaotic turbulence. The average correlation is virtually 0 for both DMD and OMD reconstructions, despite the artificial damping. A closer inspection of the time series reveals that this is due to a slight mismatch between the frequency estimated by the method and the real distinct frequency observed in the flow. It is therefore unsurprising that DMDho performs better as it is the only method that estimates the same frequency for both PIV and DIC decompositions. This does not imply that the other methods are incorrect. In fact, the relative differences between the estimated frequencies by every method is of the same order of the spectral resolution using fast Fourier transform. Nevertheless, reconstructing the signal is a significantly more demanding test. Therefore, greater accuracy in the determination of $St^\star$ is required for the data to be well reconstructed.

Considering the spatial distribution of the correlation in the DMDho case; a smaller correlation can be observed in the flow regions where shear layers appear. This result is in agreement with figure 3 where the shear layers are reported to be dominated by a distinctly different frequency. Further, as they are uncorrelated with the membrane deformation (c.f. figure 4), one would not necessarily expect the reconstruction to perform adequately in these areas. To assess the contribution of the shear layers to the spatial average the average conditioned to $St^\star = 0.75$ is computed following figure 3. By comparing the former $\langle \rho_v \rangle = 0.42$ with the conditioned $\langle \rho_v | St^\star = 0.75 \rangle = 0.45$, it is concluded that the shear layers in the global reconstruction of the flow field are not of leading order importance.

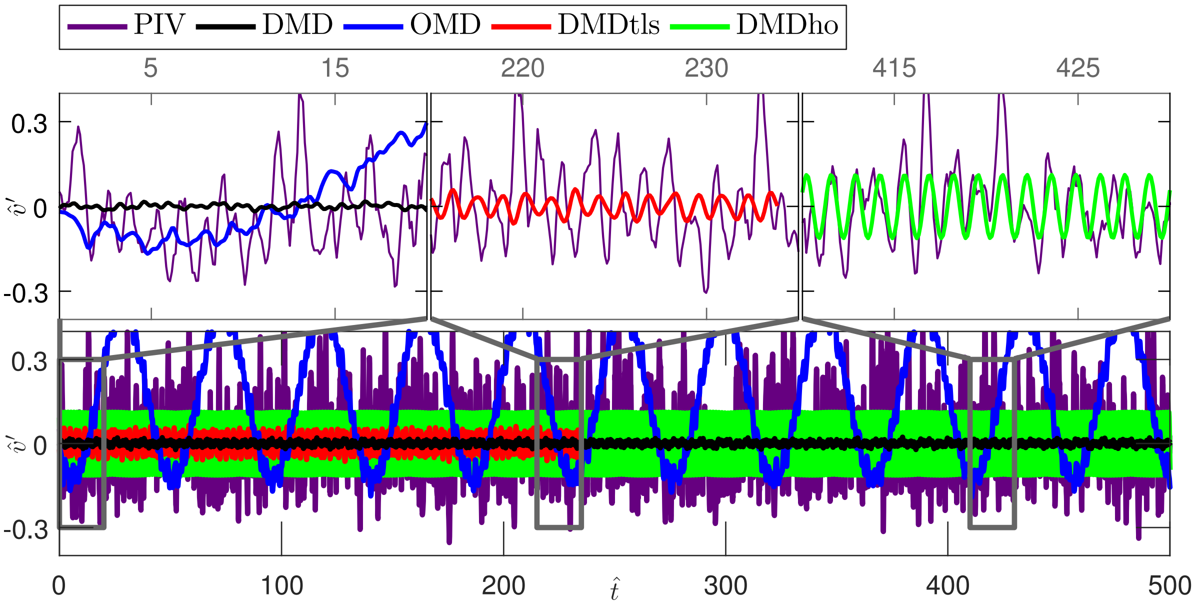

Figure 10: Normalized vertical velocity fluctuations $\hat{v}'$ at an arbitrary point ($\hat{x} = -0.2$, $\hat{y} = 0.3$, shown with a pink dot in figure 8) measured by PIV and using the various decomositions. The damping coefficients are set to $\delta = 0$. The three upper plots represent zoomed regions of the lower graph. For clarity, some lines are suppressed in these zoomed plots.

A similar analysis was performed for the membrane deformation. For brevity, the time series reconstruction (as done in figures 9 and 10 for the PIV data) is not shown. However, the problem of vanishing reconstructions persisted accordingly (as can also be inferred from $\delta < 0$ in figure 7). Therefore, the damping coefficients were set to $\delta = 0$. The fidelity of the reconstruction was quantified just as for the velocities using ρ_y as shown in figure 12. Similar conclusions can be drawn from this figure: (i) the correlation of the real and reconstructed fields is virtually 0 for DMD, OMD and DMDtls. (ii) The reconstruction is comparatively better for the $\alpha = 15°$ case. (iii) There is a significant level of correlation, i.e. a satisfactory degree of reconstruction using the DMDho method. This result is surprising in the sense that one would expect these methods to exhibit better performance for the membrane deformation as the phenomenon is intrinsically more linear with comparatively less non-linear effects due to turbulence. This may be the reason why the correlation coefficient reaches $\langle \rho_y \rangle = 0.85$ via DMDho as opposed to $\langle \rho_v \rangle = 0.42$ for the PIV case. It appears that the lack of accuracy regarding the estimation of the primary oscillating membrane frequency for the other three methods renders them unable to accurately reconstruct the membrane deformation (figure 7).

To summarize, whilst all methods considered produce a sufficiently good estimation of the flow phenomena (similar dominant modes and similar estimated $St^\star$ within frequency resolution), this is not true for the reconstruction process following equation (12). A first obstacle is encountered because the damping coefficients are estimated to be non-zero while the process is quasi-periodic. However, even avoiding this problem, the slight differences in the frequency estimation cause DMD, OMD and DMDtls to fail in the reconstruction process whereas the reconstruction using DMDho provides a satisfactory level of correlation with the original field. This correlation level is higher in the membrane deformation, likely due to it's linear nature.

We remark that although the lack of correlations may leave the impression that the methods other than DMDho fail completely, this largely stems from the choice of quantifying the reconstruction as defined in equation 13. In fact, the mode shapes (figure 8) and estimated frequencies (table 1) agree reasonably well across methods. A slight misalignment in phase due to inaccuracies in the estimated mode frequency may lead to zero correlation. An alternative quantification could account for this by shifting the reconstructions forwards and backwards in time. The present study is however focused on the efficacy of the instantaneous reconstructions without considering time lags. Nevertheless, this effect remains important in the interpretation of the presented results.

4.3 A combined fluid-structure reconstruction

Section 4.2 has shown that for the present data the only method able to provide a satisfactory reconstruction of the flow-structure interaction is DMDho. This was shown by performing two separate decompositions: one for the flow and one for the membrane. The only point where fluid-structure interaction may be inferred is

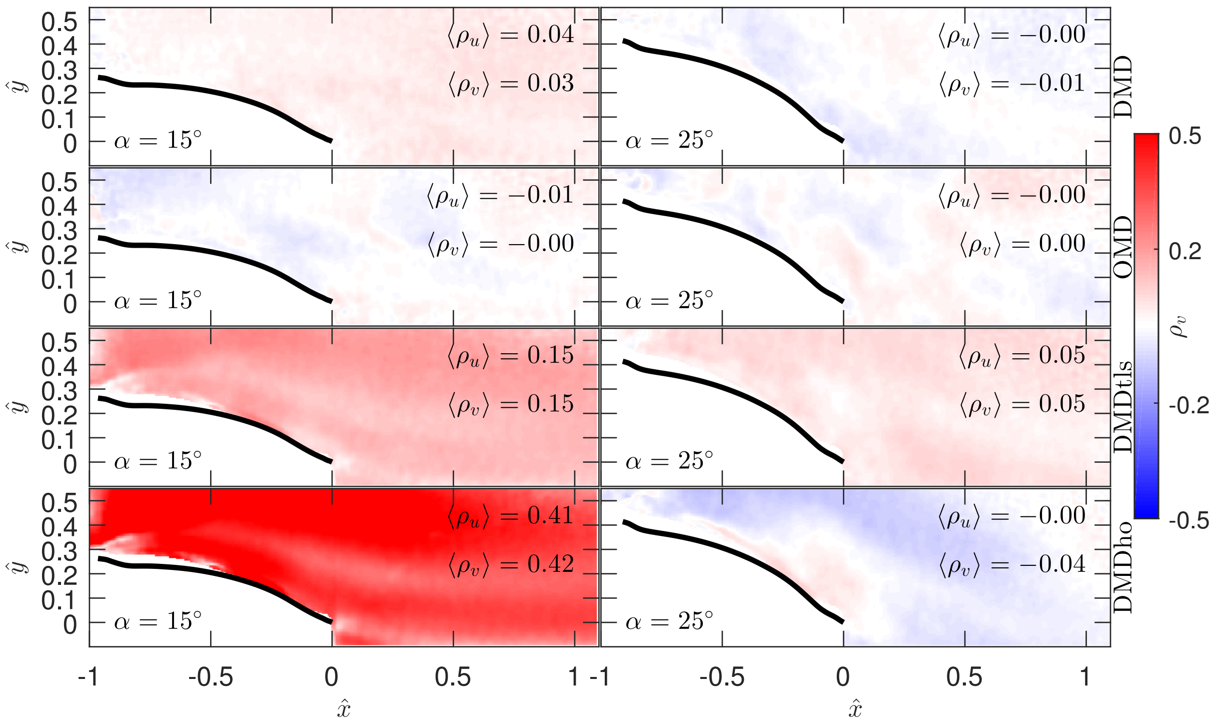

Figure 11: Correlation coefficient maps $\rho_v(\hat{x}, \hat{y})$ of the real and reconstructed fields of the vertical velocity fields for various decompositions and the two angles of attack. The legends show the numerical values of the spatial averages $\langle \rho_u \rangle$ and $\langle \rho_v \rangle$. Note that the maps of $\rho_u(\hat{x}, \hat{y})$ are not shown.

the comparison of the PIV and DIC characteristic frequencies (only 0.003% difference for the $\alpha = 15°$ case). Alternatively, instead of forming the snapshot vector $\boldsymbol{v}_j$ with only the PIV or the DIC fields (as described in section 3), one can instead generate a new snapshot by combining the PIV and the DIC fields together. In this case $\boldsymbol{v}_j \in \mathbb{R}^J$ where $J = J_{PIV} + J_{DIC} \approx 7 \times 10^4$ is twice the number of PIV vectors plus the number of DIC points. In this way, a linear model is sought that combines the flow and membrane information, taking advantage of the flexibility of DMD. As mentioned in section 1, these methods have been extensively used to retrieve information from fluid flow but they have not been applied to fluid-structure problems. Recently, Goza and Colonius (2017) considered the simulation of the flow over a flapping flag. In their study they also used a combined approach including the velocity of the structure in $\boldsymbol{v}_j$. They proposed a different weighting for the flow and structural deformations based on their respective mechanical energy. However, they only use that weighting for the computation of POD modes (as POD modes are order based on the energy content) and not in the DMD.

In the present study, this combined approach will be carried out using the DMDho method as it has clearly outperformed the other three methods. The vector $\boldsymbol{v}_j$ is formed with the PIV and DIC data (no deformation velocity or weighting are considered). Further, for consistency, the same values of $\epsilon_t = 0.02$ and $d = 300$ are maintained as in the previous cases.

The performance of the combined approach can be assessed by comparing the correlation coefficient between the real and reconstructed fields. Figure 13 presents the flow results for both separated and combined approaches. There appears to be virtually no difference between the two methodologies. Further, the same features can be observed: worse reconstruction in the shear layers where the flow is not driven by the membrane deformation, marginally better reconstruction of the vertical velocity and significantly better performance in the $\alpha = 15°$ case. The membrane deformation reconstruction is only marginally improved by using the combined approach in the $\alpha = 15°$ case ($\langle \rho_y \rangle = 0.86$ contrasting with $\langle \rho_y \rangle = 0.85$ in the separated approach).

Using the other decompositions (DMD, OMD and DMDtls), it was observed in previous sections that the frequencies estimated in the PIV or DIC cases were different (c.f. table 1). This result could potentially lead to an erroneous conclusion in which the fluid-structure coupling was neglected (especially in the $\alpha = 25°$ case where the difference was of the order of 20%). Using the combined approach, this problem could potentially be avoided as the same frequency is estimated for the fluid and structure together (which are now combined into a single mode). However, the same problems that were reported in sections 4.1 an 4.2 still remain: (i) inaccurate estimation of damping coefficient (preventing successful reconstruction). (ii) Artificially setting $\delta = 0$ does not improve the result due to inaccurate frequency estimation of the dominant periodic motions. It is therefore concluded that, although providing the same qualitative description of the flow phenomena (frequencies and

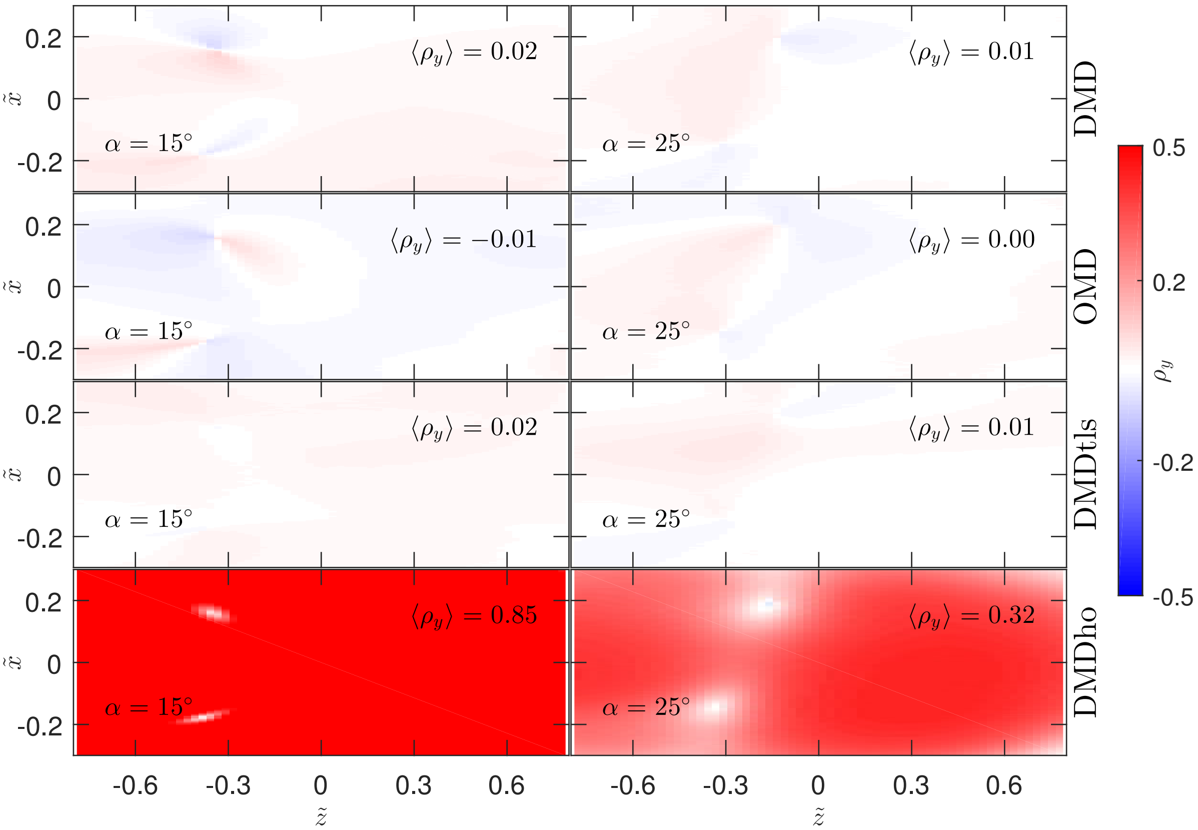

Figure 12: Correlation coefficient maps $\rho_y(\tilde{x}, \tilde{z})$ of the real and reconstructed fields of membrane deformation for various decompositions and the two angles of attack. The legends show the numerical values of the spatial average $\langle \rho_y \rangle$.

modes); these three decompositions (DMD, OMD and DMDtls) are unable to produce qualitative reconstructions of the flow-structure interaction in the present data. The fact that these decompositions fail to provide a satisfactory reconstruction of the flow field in the present case does not imply that they would fail to do so in all circumstances. In fact, it is likely that the inaccurate estimation of the frequency (which is the main source of reconstruction error) is due to the presence of measurement noise. It is therefore expected that this may change for other problems. However, the use of DMDho is expected to yield improved estimation and reconstruction based on these results.

It should be noted that DMD-based methods do not extract the flow dynamics based on their energy content. Instead, the different modes and/or frequencies are extracted based on their dynamical significance. Further, modes are associated with a flow phenomenon with the same frequency are likely to be included in the same spatial structure. For example, the lack of energy-based information enabled Baj et al. (2015) to detect and isolate wakes of small cylinders originated in the vicinity of larger wakes. Baj et al. (2015) showed that energy-based methodologies, such as POD, failed to capture small wakes due to their small relative energy content. This is the same reason why, more recently, Goza and Colonius (2017) proposed to apply a different weighting to the fluid and structure data to compensate for their unequal distribution of energy. These authors also claimed that the same weighting was not applied to their DMD case for consistency with most of the cases in the literature. It should be noted that DMD-based methods should not require energy weighting as they will detect the dynamics purely in terms of mapping one flow instant to the next through the propagator R (equation 2). Such a weighting would play a role mainly for intelligent choices of the POD subspace truncation threshold ϵ_t based on an estimation of the role played by combined uncertainty in the quantities of interest.

To test the validity of DMD independence of energy-based weighting, the relative importance of the flow and structural data can be systematically varied. The easiest way to do this is to consider only a subset of the DIC points to describe the membrane deformation. Note that, in the previous examples, the number of PIV data points ($J_{PIV} \approx 6 \times 10^4$) and the number of DIC data points ($J_{DIC} \approx 10^4$) were of the same order of magnitude. The same procedure is repeated but now reducing J_{DIC} in systematically. The membrane information was progressively reduced down to taking a single point. For consistency the performance of the method was evaluated as the spatial average of the correlation coefficient between the measured and reconstructed fields. Figure 14 shows $\langle \rho \ \rangle$ for the fluid velocity and the membrane deformation as a function of the number of data

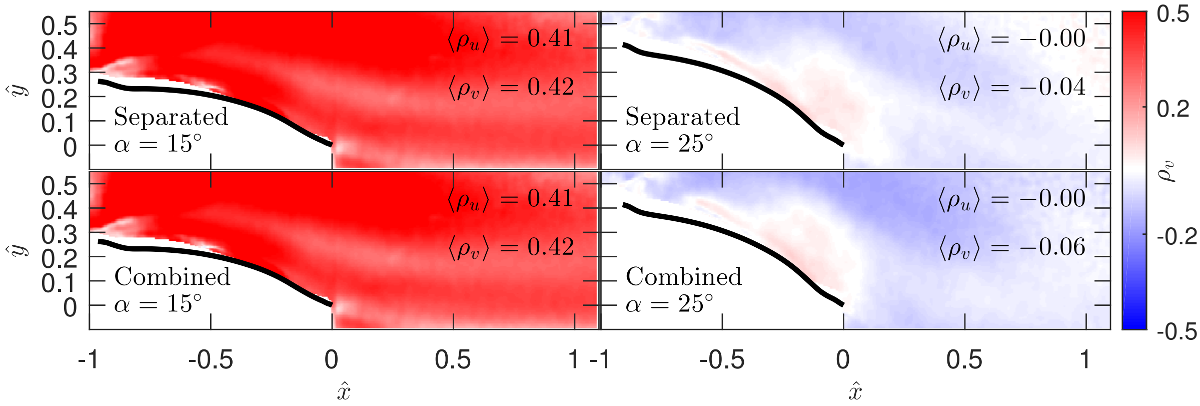

Figure 13: Correlation coefficient maps $\rho_v(\hat{x}, \hat{y})$ of the real and reconstructed fields of the vertical velocity fields for the separated and combined approaches and the two angles of attack. The legends show the numerical values of the spatial averages $\langle \rho_u \rangle$ and $\langle \rho_v \rangle$. Note that the plots in the upper row are reproduced from figure 11 to ease comparison.

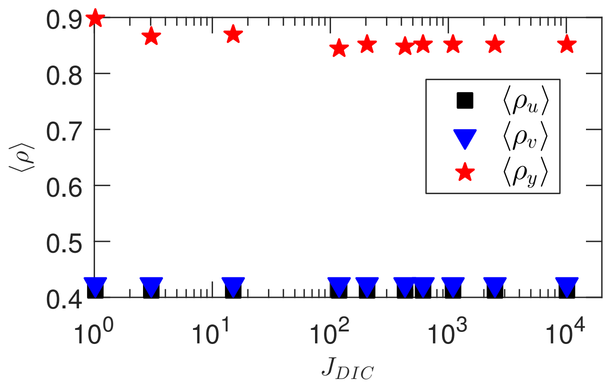

Figure 14: Spatial-averaged correlation coefficients, $\langle \rho_y \rangle$, $\langle \rho_u \rangle$ and $\langle \rho_v \rangle$ between the real and reconstructed fields of membrane deformation for the combined approaches as a function of the number of points taken used to describe the membrane deformation (J_{DIC}). Only DMDho $\alpha = 15°$ results are shown.

points describing the membrane deformation. It is clear that the performance of the method is not affected by J_{DIC}. Hence it is concluded that, as far as the flow and structural data happen at the same frequency, the performance of DMD-based methodologies is independent of the relative energy of flow and deformation.

5 Conclusions

Simultaneous measurements of flow velocity (PIV) and membrane deformation (DIC) are considered in the flow past a membrane wing at two angles of attack $\alpha = 15°$ and $\alpha = 25°$. It is observed that the majority of the flow exhibits a single dominant frequency as a consequence of the coupling between the fluid and membrane. This fluid-structure interaction was also characterized by means of the spectral coherence, γ, showing that there exists an approximately linear relationship ($\gamma \neq 0$) between the membrane deformation and the flow at a particular Strouhal number $St^{\star}$ (the dominant frequency of the flow field).

As this coupling occurs primarily at a single frequency, the problem is suitable for the application of low-order models in which each spatial mode is uniquely associated with a temporal frequency. Consequently, the suitability of four such models (DMD, OMD, DMDtls and DMDho) were tested. As a first approach, these methodologies were applied to the flow field and membrane deformation separately. It was shown that the dominant mode/frequency pair selection is not straightforward due to the sensitive estimation of the damping coefficients. Their inaccuracy implied that the flow reconstruction either vanishes ($\delta < 0$) or tends to infinity ($\delta > 0$); compromising the reconstruction. Nevertheless, the four decompositions provided the same qualitative flow description and the spatial modes were similar. Furthermore, the dominant frequencies estimated by the various decompositions coincided within the same frequency resolution of the Fourier transform (though the precision of that estimation proved very important in the quality of the reconstructions). Using this methodology, the degree of fluid-structure interaction was assessed by comparing the dominant frequencies of the PIV and DIC fields. DMD, OMD and DMDtls exhibited similar behaviour: when the interaction was stronger ($\alpha = 15°$) the estimated dominant frequencies varied less than 3% and when the interaction was weaker ($\alpha = 25°$) the PIV and DIC frequencies differed up to 20%. On the other hand, DMDho performed better than the other three decompositions and the estimated frequencies differed less than 0.1% independently of α. Moreover, the damping coefficients estimated by DMDho were sufficiently close to 0; avoiding the problem of reconstructions vanishing or tending to infinity.

The flow and membrane deformation reconstruction was assessed by means of the average temporal correlation between the measured and reconstructed fields. This was shown to be virtually 0 for the DMD, OMD and DMDtls decompositions. This was due to (i) inaccurate estimation of the damping coefficients, $\delta \neq 0$, and (ii) the imprecise estimation of the dominant frequency. It was demonstrated that although the former can be improved by artificially setting $\delta = 0$, the latter problem prevailed and the reconstruction was unsuccessful. In contrast, DMDho resulted in $\langle \rho_v \rangle = 0.42$ and $\langle \rho_y \rangle = 0.85$ in the $\alpha = 15°$ case. This implies that the flow and the membrane deformation are reconstructed with satisfactory accuracy with this method.

The difference in dominant frequency of the PIV and DIC cases can be avoided by using a combined approach in which the low-order model is applied to a combined snapshot containing both the PIV velocities and the DIC deformations. However, it was found that doing so did not circumvent the imprecise estimation of the dominant frequency. DMDho remained the only decomposition able to provide a satisfactory reconstruction. By taking a smaller subset of the membrane deformation data points it was shown that, as opposed to previous approaches based on energy content (POD), this methodology enables a satisfactory reconstruction of the problem independently of the relative energy of the fluid and membrane deformation.

Acknowledgements

The authors gratefully acknowledge funding from H2020 Project HOMER (Project No 769237). The results from the presented figures are available for download at `https://doi.org/10.5258/SOTON/D1751`.

References

Bagheri, S. (2014). Effects of weak noise on oscillating flows: Linking quality factor, floquet modes, and koopman spectrum. *Physics of Fluids*, 26(9):094104.

Baj, P., Bruce, P. J. K., and Buxton, O. R. H. (2015). The triple decomposition of a fluctuating velocity field in a multiscale flow. *Physics of Fluids*, 27(7):075104.

Barbu, I.A., de Kat, R., and Ganapathisubramani, B. (2017). Aerodynamic step input response of electro-active membrane wings. in *25th AIAA/AHS Adaptive Structures Conference Forum 2017-0056*, Grapevine, Texas, USA.

Berkooz, G., Holmes, P., and Lumley, J. L. (1993). The Proper Orthogonal Decomposition in the Analysis of Turbulent Flows. *Ann. Rev. Fluid Mech.*, 25:539–575.

Bleischwitz, R., de Kat, R., and Ganapathisubramani, B. (2015). Aspect-Ratio Effects on Aeromechanics of Membrane Wings at Moderate Reynolds Numbers. *AIAA Journal*, 53(3):780–788.

Bleischwitz, R., de Kat, R., and Ganapathisubramani, B. (2016). Aeromechanics of membrane and rigid wings in and out of ground-effect at moderate Reynolds numbers. *Journal of Fluids and Structures*, 62:318–331.

Bleischwitz, R., de Kat, R., and Ganapathisubramani, B. (2017). On the fluid-structure interaction of flexible membrane wings for MAVs in and out of ground-effect. *Journal of Fluids and Structures*, 70(October 2016):214–234.

Bozkurttas, M., Mittal, R., Dong, H., Lauder, G. V., and Madden, P. (2009). Low-dimensional models and performance scaling of a highly deformable fish pectoral fin. *Journal of Fluid Mechanics*, 631:311–342.

Buoso, S. and Palacios, R. (2016). Viscoelastic effects in the aeromechanics of actuated elastomeric membrane wings. *Journal of Fluids and Structures*, 63:40–56.

Curet, O. M., Carrere, A., Waldman, R., and Breuer, K. S. (2014). Aerodynamic Characterization of a Wing Membrane with Variable Compliance. *AIAA Journal*, 52(8):1749–1756.

Dawson, S. T. M., Hemati, M. S., Williams, M. O., and Rowley, C. W. (2016). Characterizing and correcting for the effect of sensor noise in the dynamic mode decomposition. *Experiments in Fluids*, 57(3):1–19.

Eckart, C. and Young, G. (1936). The approximation of one matrix by another of lower rank. *Psychometrika*, 1(3):211–218.

Goza, A. and Colonius, T. (2017). Modal decomposition of fluid-structure interaction with application to flag flapping. *arXiv:1171.03040v1 [physics.flu-dyn]*.

Jovanović, M. R., Schmid, P. J., and Nichols, J. W. (2014). Sparsity-promoting dynamic mode decomposition. *Physics of Fluids*, 26(2):024103.

Kim, D., Cossé, J., Huertas Cerdeira, C., and Gharib, M. (2013). Flapping dynamics of an inverted flag. *Journal of Fluid Mechanics*, 736:1–12.

Le Clainche, S. and Vega, J. M. (2017). Higher Order Dynamic Mode Decomposition. *SIAM Journal on Applied Dynamical Systems*, 16(2):882–925.

Le Clainche, S., Vega, J. M., and Soria, J. (2017). Higher order dynamic mode decomposition of noisy experimental data: The flow structure of a zero-net-mass-flux jet. *Experimental Thermal and Fluid Science*, 88:336–353.

Menon, K. and Mittal, R. (2020). Dynamic mode decomposition based analysis of flow over a sinusoidally pitching airfoil *Journal of Fluids and Structures*, 94:102886

Rodríguez-López, E., Bruce, P. J. K., and Buxton, O. R. H. (2016). Near field development of artificially generated high Reynolds number turbulent boundary layers. *Physical Review Fluids*, 1(7):074401.

Rojratsirikul, P., Genc, M. S., Wang, Z., and Gursul, I. (2011). Flow-induced vibrations of low aspect ratio rectangular membrane wings. *Journal of Fluids and Structures*, 27(8):1296–1309.

Rowley, C. W. and Dawson, S. T. (2017). Model Reduction for Flow Analysis and Control. *Annual Review of Fluid Mechanics*, 49(1):387–417.

Schmid, P. J. (2010). Dynamic mode decomposition of numerical and experimental data. *Journal of Fluid Mechanics*, 656:5–28.

Thomareis, N. and Papadakis, G. (2017). Effect of trailing edge shape on the separated flow characteristics around an airfoil at low reynolds number: A numerical study. *Physics of Fluids*, 29(1):014101.

Wynn, A., Pearson, D. S., Ganapathisubramani, B., and Goulart, P. J. (2013). Optimal mode decomposition for unsteady flows. *Journal of Fluid Mechanics*, 733:473–503.

Zheng, Z.C., and Zhang, N. (2008). Frequency effects on lift and drag for flow past an oscillating cylinder *Journal of Fluids and Structures*, 24(3):382-399